Materials Advances

PAPER

View Article Online
View Journal

Check for updates

Cite this: DOI: 10.1039/d6ma00031b

Facile synthesis of ultralow-band-gap alkoxythiophene-flanked diketopyrrolopyrrole homopolymers *via* $FeCl_3$-mediated oxidative polymerization

Samala Venkateswarlu,[a] Ravinder Singh,[a] Songbo Cui,[a] Andrew Stella,[a] Jimmy Papazotos,[a] Naixin Zhao,[a] Yi Yuan,[a] Haitao Liu,[b] Xu Li,[b] Jinliang Wang[b] and Yuning Li *[a]

Received 7th January 2026,
Accepted 16th April 2026

DOI: 10.1039/d6ma00031b

rsc.li/materials-advances

Conjugated polymers with strong absorption in the near-infrared-II (NIR-II, 1000–1700 nm) region are highly attractive for optoelectronic and biomedical applications. However, their availability remains limited, and their synthesis often relies on costly transition-metal catalysts and multistep monomer functionalization. Here, we report an economical and operationally simple $FeCl_3$-mediated oxidative polymerization strategy for the synthesis of two alkoxythiophene-flanked diketopyrrolopyrrole (DPP) homopolymers, $PDPPC_{20}OT\text{-}C_8$ and $PDPPC_{12}OT\text{-}C_{12}$. Both polymers exhibit intense NIR-II absorption, with maximum absorption wavelengths reaching ∼1190 nm, and ultralow optical band gaps as low as 0.87 eV. Side-chain engineering enables good solubility, suppressed crosslinking, and more coplanar backbone conformation, leading to ambipolar charge transport in organic thin-film transistors. Optimized devices based on $PDPPC_{12}OT\text{-}C_{12}$ show balanced hole and electron mobilities of up to 1.74×10^{-3} and 2.24×10^{-3} $cm^2\ V^{-1}\ s^{-1}$, respectively. Density functional theory calculations reveal enhanced backbone planarity arising from intramolecular S···O interactions, consistent with the experimentally observed red-shifted absorption and reduced band gaps. This work establishes $FeCl_3$-mediated oxidative polymerization as a viable route to high-performance ultralow-band-gap DPP homopolymers and highlights their potential for ambipolar thin film transistors, NIR-II photodetection, and photothermal applications.

1. Introduction

Over the years, π-conjugated polymers (CPs) have attracted significant interest in organic electronics owing to their unique optoelectronic properties. They have been explored for a wide range of applications, including organic thin-film transistors (OTFTs) or organic field-effect transistors (OFETs), organic light-emitting diodes (OLEDs), organic photo-detectors (OPDs), organic solar cells (OSCs), transparent electrodes, thermoelectric and electrochromic devices.[1–10] CPs with low band gaps that exhibit strong absorption in the near-infrared (NIR) region are of particular interest, as they often display ambipolar charge transport and are promising for biomedical imaging and NIR photodetectors.[11–14] Among various molecular design strategies, the donor–acceptor (D–A) approach has emerged as the most widely adopted for achieving low-band-gap CPs.[15–18] Incorporation of strong donor and acceptor units in the CPs raises the highest occupied molecular orbitals (HOMO) while lowering the lowest unoccupied molecular orbitals (LUMO), thereby effectively reducing the band gap. Band gap narrowing extends optical absorption into the NIR region and enables ambipolar charge transport.[19–21] For biological imaging applications, the NIR-II window (1000–1700 nm) is preferred over the NIR-I window (700–900 nm) because it enables efficient tissue penetration and improved spatial resolution.[22–24] Despite these advantages, only a limited number of conjugated polymers exhibit maximum absorption wavelengths (λ_{max}) in the NIR-II regime.[25]

Thiophene-flanked diketopyrrolopyrrole (DPPT) is one of the most widely used electron-acceptor building blocks for constructing D–A polymers.[26–31] Coupling DPPT with strong donor comonomers, such as alkoxythiophenes, effectively narrows the band gap and redshifts the λ_{max} to approximately 900 nm.[25] However, this absorption remains within the NIR-I region. An alternative and more effective strategy is to pair DPPT with strong electron-acceptor comonomers. Benzobisthiadiazole (BBT),[30] thienoisoindigo,[32] and dioxothienopyrrolebenzodifurandione (BTPBF)[33] have each been

---

[a] Department of Chemical Engineering and Waterloo Institute for Nanotechnology (WIN), University of Waterloo, Waterloo, Ontario N2L 3G1, Canada. E-mail: yuning.li@uwaterloo.ca

[b] Institute of Chemistry, Henan Academy of Sciences, 56 Hongzhuan Road, Jinshui District, Zhengzhou, Henan 450002, China

demonstrated to significantly extend polymer absorption into the NIR-II region. Stille and Suzuki C–C coupling polymerization methods using Pd catalysts have been used to synthesize these polymers.

More recently, efforts have made to replace the flanking thiophenes of DPP with the more electron-rich 4-methoxythiophene to further reduce the optical band gap. Domokos *et al.*[34] synthesized a series of homo- and copolymers based on 2-hexyldecyl-substituted DPP flanked by 4-methoxythiophene (DPPC$_1$OT) units and observed pronounced redshifts relative to their thiophene-flanked counterparts. The homopolymer PDPP-2T-OMe exhibited λ_{max} values of 1019 nm in solution and 998 nm in thin film. Giri *et al.*[35] reported a structurally related homopolymer (P3) derived from DPPC$_1$OT bearing longer 2-octyldodecyl side chains on the DPP unit, which displayed λ_{max} values of ~1000 nm in both solution and thin films and showed promise as an energy-efficient infrared electrochromic optical attenuator. Collectively, these studies indicate that homopolymers derived from DPPC$_1$OT are promising semiconductor materials for NIR-II photodetection. However, their charge transport properties have not yet been investigated. In addition, both studies relied on Yamamoto coupling of dibrominated monomers using bis(1,5-cyclooctadiene)nickel(0) (Ni(COD)$_2$), which is costly and suffers from limited thermal and chemical stability. Consequently, the development of a more economical and operationally simple polymerization strategy remains highly desirable.

In this study, we first attempted to synthesize the homopolymer PDPPC$_1$OT-C$_{20}$ (Scheme 1), which corresponds to P3 reported by Giri *et al.*,[35] *via* FeCl$_3$-mediated oxidative polymerization of the non-brominated monomer M2. However, the resulting polymer was completely insoluble in common organic solvents, which is primarily attributed to the crosslinking side reactions during polymerization. To improve solubility, the long, branched 2-octyldodecyl side chains were relocated from the DPP core to the flanking thiophenes to replace the methyl substituents, while the DPP unit was substituted with 1-octyl side chains to afford a redesigned monomer, M3. The corresponding polymer, PDPPC$_{20}$OT-C$_8$, prepared by FeCl$_3$ oxidative polymerization, exhibited good solubility in chloroform, chlorobenzene, and 1,2-dichlorobenzene. In addition, a second redesigned monomer, M4, a 4-dodecyloxythiophene-flanked DPP bearing 2-butyloctyl side chains, was synthesized. Polymerization of M4 under identical conditions yielded another soluble homopolymer, PDPPC$_{12}$OT-C$_{12}$.

PDPPC$_{20}$OT-C$_8$ exhibits λ_{max} values of 1035 nm in solution and 1190 nm in thin films, whereas PDPPC$_{12}$OT-C$_{12}$ shows λ_{max} values of 1176 nm in solution and 1186 nm in thin films. All of these absorption maxima fall within the NIR-II regime. Notably, these λ_{max} values are substantially redshifted relative to previously reported DPPC$_1$OT homopolymers,[34,35] indicating more extended π-conjugation. This enhancement is likely associated with improved backbone planarity induced by long alkoxy side chains on the thiophene units, which reduce backbone rotational freedom. When used as the semiconducting channel layers in OTFTs, both polymers display ambipolar charge transport with well-balanced hole and electron mobilities reaching approximately 10^{-3} cm^2 V^{-1} s^{-1}.

2. Experimental

2.1 Synthesis of poly(2,5-bis(2-octyldodecyl)-3,6-di(thiophen-2-yl)-2,5-dihydropyrrolo[3,4-*c*]pyrrole-1,4-dione) (PDPPT-C$_{20}$)

Anhydrous FeCl$_3$ (65 mg, 0.40 mmol) and chlorobenzene (3 mL) were placed in a 25 mL oven-dried two-necked round-bottom

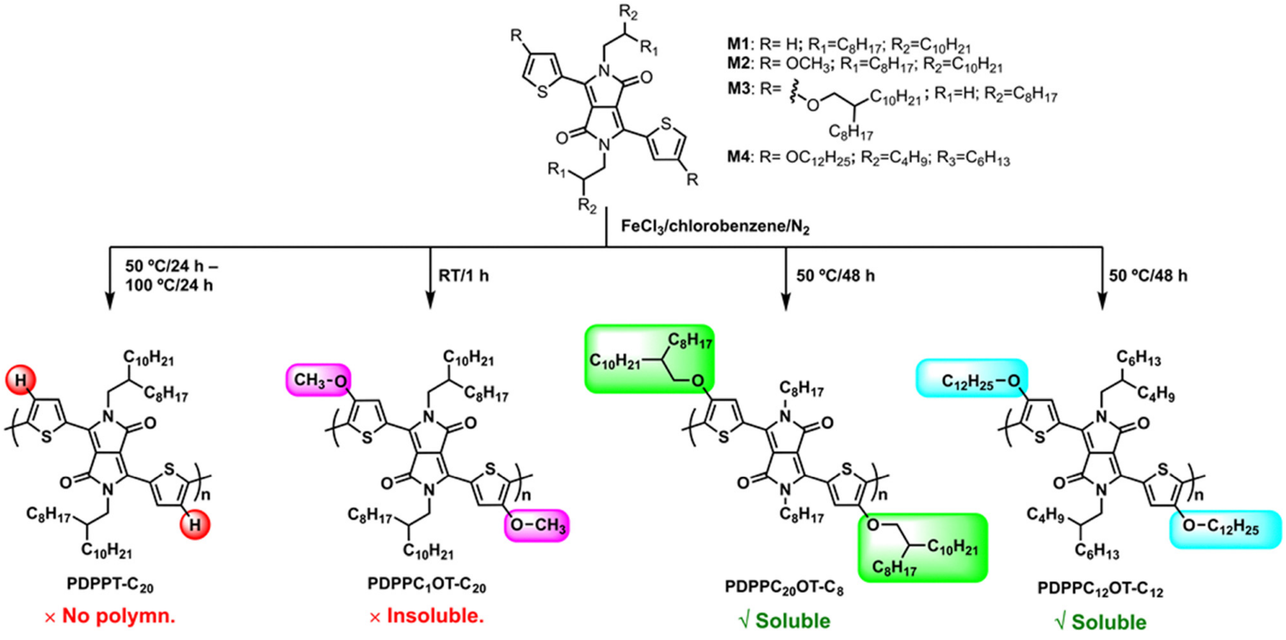

Scheme 1 Synthesis of DPP homopolymers *via* FeCl$_3$-mediated oxidative polymerization.

flask and stirred for 5 min under a nitrogen atmosphere. A solution of M1 (86.2 mg, 0.1 mmol) in chlorobenzene (1 mL) was added dropwise *via* syringe at room temperature, after which the reaction mixture was heated to 50 °C and stirred for 24 h. The reaction temperature was then increased to 100 °C and the mixture was stirred for an additional 24 h. Upon completion, the solvent was removed under reduced pressure using a rotary evaporator, and the crude product was precipitated by the addition of methanol. The precipitate was collected by filtration and washed several times with methanol. Further purification was performed by Soxhlet extraction using acetone followed by hexane. Most of the material was extracted with acetone, and the remaining solid was completely dissolved in hexane. Evaporation of the hexane fraction afforded a bluish solid in 3% yield (2.6 mg).

2.2 Synthesis of poly(3,6-bis(4-methoxythiophen-2-yl)-2,5-bis(2-octyldodecyl)-2,5-dihydropyrrolo[3,4-*c*]pyrrole-1,4-dione) (PDPPC$_1$OT-C$_{20}$)

Anhydrous $FeCl_3$ (65 mg, 0.40 mmol) and dry chlorobenzene (3 mL) were placed in a 25 mL oven-dried two-necked round-bottom flask and stirred for 5 min under a nitrogen atmosphere at 0 °C. A solution of monomer M2 (92.2 mg, 0.1 mmol) in chloroform (1 mL) was added *via* syringe. The reaction mixture was allowed to warm to room temperature and stirred for 1 h. The mixture was poured into methanol, and the resulting precipitate was collected by filtration and washed thoroughly with methanol. The crude polymer was dedoped by stirring in methanol (50 mL) containing triethylamine (3.5 mL) for 24 h at room temperature. After filtration, washing with methanol, and drying, PDPPC$_1$OT-C$_{20}$ was obtained as a dark bluish-green solid, insoluble in common organic solvents, in 95% yield (85.7 mg).

2.3 Synthesis of poly(2,5-dioctyl-3,6-bis(4-((2-octyldodecyl)oxy)thiophen-2-yl)-2,5-dihydropyrrolo[3,4-*c*]pyrrole-1,4-dione) (PDPPC$_{20}$OT-C$_8$)

Anhydrous $FeCl_3$ (65 mg, 0.4 mmol) and dry chlorobenzene (3 mL) were added to a 25 mL oven-dried two-necked round-bottom flask and stirred for 5 min under a nitrogen atmosphere at 0 °C. A solution of monomer M3 (112 mg, 0.10 mmol) in dry chlorobenzene (1 mL) was added *via* syringe at 0 °C. The reaction mixture was then heated to 50 °C and stirred for 48 h. After completion, the reaction mixture was poured into methanol (100 mL) and stirred for 30 min. The precipitate was collected by filtration and dedoped by stirring in methanol (50 mL) containing triethylamine (3.5 mL) for 24 h at room temperature. After filtration and washing with methanol, the material was dissolved in chloroform and passed through a Celite pad to remove residual catalyst, followed by solvent removal under reduced pressure. The resulting polymer was further purified by Soxhlet extraction using acetone, hexane, and chloroform as eluents to afford PDPPC$_{20}$OT-C$_8$ as a dark bluish-green solid in 70% yield (76.9 mg). ^{1}H NMR ($CDCl_3$, 300 MHz) δ: 9.23–9.18 (br, thienyl proton), 4.45–4.22 (m, –N–CH$_2$–, –O–CH$_2$–), 2.02–1.91 (m, –CH<, –CH$_2$–), 1.25 (br, alkyl protons), 0.88 (br, –CH$_3$).

2.4 Synthesis of poly(2,5-bis(2-butyloctyl)-3,6-bis(4-(dodecyloxy)thiophen-2-yl)-2,5-dihydropyrrolo[3,4-*c*]-pyrrole-1,4-dione) (PDPPC$_{12}$OT-C$_{12}$)

Anhydrous $FeCl_3$ (65 mg, 0.40 mmol) and dry chlorobenzene (3 mL) were placed in a 25 mL oven-dried two-necked round-bottom flask under nitrogen atmosphere and cooled to 0 °C. A solution of monomer M4 (100.6 mg, 0.1 mmol) in dry chlorobenzene (1 mL) was added *via* syringe at 0 °C. The reaction mixture was heated to 50 °C and stirred for 48 h. After completion, reaction mixture was poured into methanol and stirred for 30 min, followed by filtration. The resulting solid was dedoped by stirring in methanol (50 mL) containing triethylamine (3.5 mL) for 24 h at room temperature. After filtration and washing with methanol, the material was dissolved in chloroform and passed through a Celite pad to remove residual catalyst, and the solvent was removed under reduced pressure to afford the crude product. Further purification by Soxhlet extraction using acetone, hexane, and chloroform as eluents yielded PDPPC$_{12}$OT-C$_{12}$ a dark bluish-green solid in 71% yield (71.4 mg). ^{1}H NMR ($CDCl_3$, 300 MHz) δ: 9.31–9.06 (m, thienyl proton), 4.50–4.21 (m, –N–CH$_2$–, –O–CH$_2$–), 2.02–1.87 (m, –CH<, –CH$_2$–), 1.31–1.25 (br, alkyl protons), 0.88 (br, –CH$_3$).

3. Results and discussion

3.1 Synthesis of DPP homopolymers *via* FeCl$_3$-mediated oxidative polymerization

DPP monomers M2, M3, and M4, in which the DPP core is flanked by 4-alkoxythiophene units, were synthesized, as detailed in the SI. Compared with the reference monomer M1, in which the DPP unit is flanked by unsubstituted thiophenes, the introduction of alkoxy substituents would significantly increase the electron richness of the thiophene rings and thereby enhances the susceptibility of the 5-position toward oxidative coupling. $FeCl_3$ has been widely employed as an oxidant for the synthesis of polythiophenes *via* oxidative polymerization of electron-rich thiophene monomers.[36–38] When $FeCl_3$ was applied to M1, no successful polymerization was observed. After stirring at 50 °C, followed by an additional 24 h at 100 °C, only a sticky bluish solid was obtained in a low yield of 3% (Fig. S4), which is highly soluble in hexane indicating the formation of low-molecular-weight oligomers rather than polymers. A similar observation was reported by Charyton *et al.*[39] for $FeCl_3$-mediated oxidative chemical vapor deposition polymerization of N-unsubstituted DPP flanked by unsubstituted thiophene units. The poor reactivity of M1 can be attributed to the strong electron-withdrawing nature of the DPP unit, which deactivates the thiophene rings by increasing their oxidation potential.[40,41]

In contrast, introduction of electron-donating alkoxy substituents on the thiophene units in M2–M4 lowers the oxidation potential and stabilizes the cation radical during oxidative polymerization.[42,43] Indeed, M2 underwent rapid polymerization with $FeCl_3$ at room temperature, yielding a dark bluish-green solid in 95% yield after purification (Fig. S4). However, the resulting PDPPC$_1$OT-C$_{20}$ is completely insoluble in common organic solvents. Even after heating in 1,2,4-trichlorobenzene (TCB) under stirring at temperatures up to 200 °C for 8 h, the polymer remained largely undissolved (Fig. S5). Since the same polymer prepared by Yamamoto coupling was reported to be readily soluble in chloroform at room temperature and TCB at 120 °C, the poor solubility of PDPPC$_1$OT-C$_{20}$ is likely due to the formation of crosslinked structures *via* coupling at the 3-position of the thiophene units.[44] This interpretation is further supported by the highly disordered structure of this polymer observed by powder X-ray diffraction (Fig. S6).

To improve solubility and suppress potential crosslinking, monomer M3 was designed with bulky branched 2-octyldodecyl side chains on the thiophene units and linear octyl side chains on the DPP core. These sterically demanding substituents were expected to enhance solubility and reduce undesired side reactions. Compared with M2, M3 exhibited reduced reactivity, yielding only oligomeric products after 24 h at room temperature. Therefore, the polymerization temperature was increased to 50 °C and the reaction time was extended to 48 h. Under these conditions, the target polymer PDPPC$_{20}$OT-C$_8$ was obtained as a dark bluish-green solid (Fig. S4) in a yield of 70% after purification. This polymer is readily soluble in chloroform, chlorobenzene, and 1,2-dichlorobenzene. High-temperature gel permeation chromatography (HT-GPC) revealed a weight-average molecular weight (M_w) of 54.3 kDa and a dispersity ($Đ$) of 3.17 (Fig. S34 and Table 1). The good solubility and relatively narrow molecular weight distribution suggest minimal crosslinking during polymerization.

Monomer M4, bearing less bulky linear dodecyl side chains on the thiophene units and 2-butyloctyl substituents on the DPP core, was also polymerized under identical conditions at 50 °C for 48 h. The corresponding polymer, PDPPC$_{12}$OT-C$_{12}$, was obtained in a comparable yield of 71% after purification. This polymer exhibits a lower M_w of 25.3 kDa with a dispersity of 2.91 and shows good solubility in chloroform, chlorobenzene, and 1,2-dichlorobenzene. These results indicate that long alkoxy-substituted thiophene units are effective in promoting oxidative polymerization while simultaneously suppressing crosslinking side reactions.

Thermo-gravimetric analysis (TGA) revealed decomposition temperatures of 333 °C for PDPPC$_{20}$OT-C$_8$ and 350 °C for PDPPC$_{12}$OT-C$_{12}$ (Fig. S1), confirming their good thermal stability.

3.2 Optical and electrochemical properties

The optical properties of PDPPC$_{20}$OT-C$_8$ and PDPPC$_{12}$OT-C$_{12}$ were investigated by UV-vis-NIR spectroscopy in chloroform solution and as-cast thin films on quartz substrate (Fig. 1a), and the corresponding data are summarized in Table 1. PDPPC$_{20}$OT-C$_8$ shows a pronounced spectral change upon film formation, with the apparent absorption maximum (λ_{max}) shifting from 1035 nm in solution to 1190 nm in the thin film. More specifically, the solution spectrum exhibits a main band at 1035 nm with a pronounced shoulder at 1190 nm, whereas in the film the relative intensities of these two features are reversed, giving a dominant peak at 1190 nm and a shoulder at 1035 nm. These two low-energy bands, both located in the NIR-II region, can be assigned to the 0–0 transition at longer wavelength and the 0–1 vibronic transition at shorter wavelength, associated with the intramolecular charge-transfer transition from the donor bithiophene units to the DPP acceptor units.

The large red shift in λ_{max} and the reversal in the relative intensities of the 0–0 and 0–1 bands indicate a substantial change in chain conformation and intermolecular organization from solution to the solid state. In solution, the relatively strong 0–1 transition suggests that the polymer chains are more conformationally relaxed and less planar due to good solvation by chloroform and the steric effect of the long branched C20 side chains. Upon film formation, solvent removal promotes closer interchain packing and enhanced π–π interactions, while also restricting torsional motion and increasing backbone planarization. As a result, the effective conjugation length increases, leading to the marked bathochromic shift. In addition, the dominance of the 0–0 transition in the film and the 0–1/0–0 intensity ratio below unity are consistent with J-aggregate-like character,[45,46] further supporting stronger interchain donor–acceptor interactions and a more ordered solid-state packing structure.

In contrast, PDPPC$_{12}$OT-C$_{12}$ exhibits λ_{max} values of 1176 nm in solution and 1186 nm in the solid state, both of which are attributed to the 0–0 transition, with only a small redshift of 10 nm upon film formation. Unlike PDPPC$_{20}$OT-C$_8$, the solution spectrum of PDPPC$_{12}$OT-C$_{12}$ is dominated by the 0–0 transition, indicating that significant aggregation is already present in solution. This behavior is consistent with the stronger aggregation tendency of PDPPC$_{12}$OT-C$_{12}$, likely arising from its more coplanar backbone and the reduced steric hindrance provided by the linear dodecyloxy side chains on the thiophene units together with the shorter branched side chains on the DPP core. These structural features are less effective at preventing interchain association than the longer branched side chains in PDPPC$_{20}$OT-C$_8$. As a result, PDPPC$_{12}$OT-C$_{12}$ likely exists as pre-aggregated species in solution, as commonly

Table 1 Summary of molecular weights, optical and electrochemical properties of PDPPC$_{20}$OT-C$_8$ and PDPPC$_{12}$OT-C$_{12}$

					λ_{max} [nm]		λ_{onset} [nm]	$E_g^{opt\,c}$ [eV]	$E_{HOMO}{}^d$ [eV]	$E_{LUMO}{}^d$ [eV]
Homo polymer	$M_n{}^a$ [kDa]	$M_w{}^a$ [kDa]	$Đ$	$T_d{}^b$ [°C]	Solution	Film	Film	Film	Film	Film
PDPPC$_{20}$OT-C$_8$	17.1	54.3	3.17	333	1035	1190	1375	0.90	−5.06	−4.16
PDPPC$_{12}$OT-C$_{12}$	8.7	25.3	2.91	350	1176	1186	1425	0.87	−5.02	−4.15

[a] Measured from HT-GPC using 1,2,4-trichlorobenzene as eluent at 150 °C. [b] Thermal decomposition temperatures (T_d) at 5% weight loss. [c] Optical band gaps ($E_g^{opt's}$) calculated from the onset absorption wavelengths of the thin films. [d] E_{HOMO} of polymers were calculated using their onset oxidation potentials, with ferrocene as a reference ($E_{HOMO} = -4.8$ eV), while $E_{LUMO's}$ of polymers were calculated using the equation: $E_{LUMO} = E_g^{opt} + E_{HOMO}$.

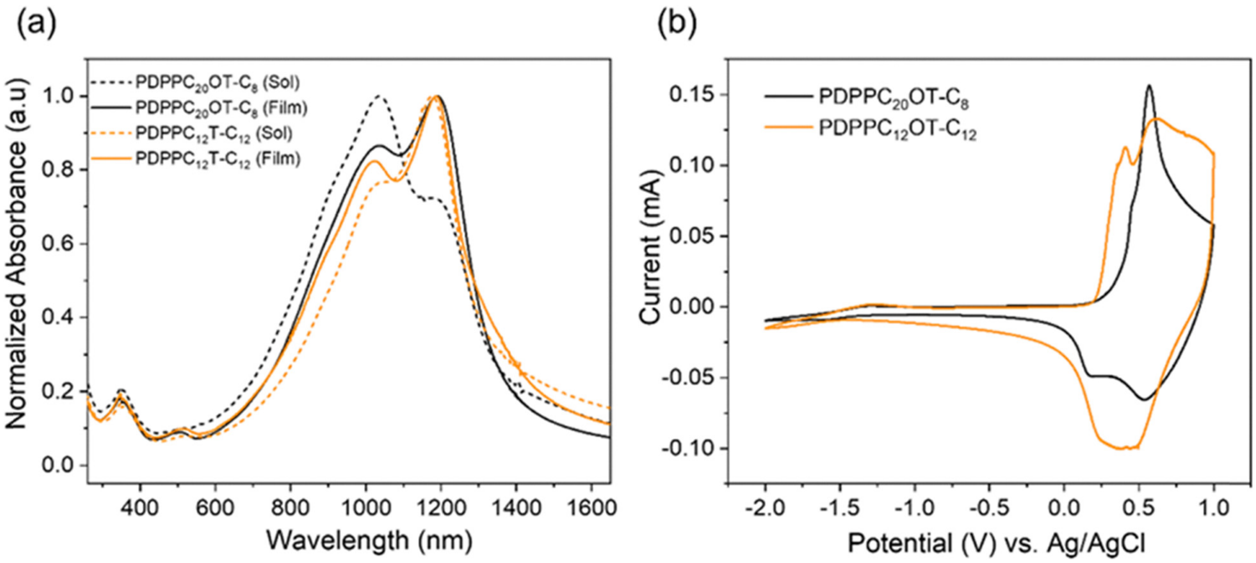

Fig. 1 (a) Normalized UV-vis-NIR absorption spectra of PDPPC$_{20}$OT-C$_8$ and PDPPC$_{12}$OT-C$_{12}$ measured in chloroform solution and as-cast thin films. (b) Cyclic voltammograms of PDPPC$_{20}$OT-C$_8$ and PDPPC$_{12}$OT-C$_{12}$ thin films recorded in 0.1 M Bu$_4$NPF$_6$ in dry acetonitrile at a scan rate of 50 mV s^{-1}.

reported for DPP-based polymers with strong intermolecular interactions.[47] Therefore, its solution absorption spectrum already resembles that of the solid film, and only a minimal additional red shift is observed upon film formation.

The optical band gaps of PDPPC$_{20}$OT-C$_8$ and PDPPC$_{12}$OT-C$_{12}$ were estimated to be 0.90 eV and 0.87 eV, respectively, based on the onset absorption wavelenghts of their thin films. Compared with previously reported homopolymers of 4-methoxythiophene-flanked DPP (DPPC$_1$OT),[34,35] both polymers exhibit substantially redshifted absorption maxima and narrower optical band gaps. The shorter $\lambda_{\max}$ (998 nm) reported by Domokos *et al.*[34] may be attributed to the low molecular weight of the polymer (M_w = 2.9 kDa). However, even the higher-molecular-weight polymer (M_w = 87.7 kDa) reported by Giri *et al.*[35] displayed a $\lambda_{\max}$ of only ~1000 nm. These observations suggest that replacing the methyl substituents on the methoxythiophene units with longer linear or branched alkyl chains significantly extends the effective conjugation length in DPP homopolymers. Such long alkyl side chains can pack more tightly in the solid state, restricting the rotational freedom of thiophene units along the polymer backbone and promoting a more coplanar conformation, whereas smaller methyl substituents are more mobile and contribute less effectively to backbone planarity.[48]

Most CPs exhibited $\lambda_{\max}$ either in visible (400–780 nm) or NIR I (780–1000 nm) regions, whereas polymers with $\lambda_{\max}$ in NIR-II region remain rare.[25] Notably, in this work, both newly prepared polymers display absorption maxima in the NIR-II window. Even more importantly, these polymers exhibit very weak π–π* absorption in the visible region compared with their strong absorption in the NIR-I and NIR-II regions, resulting in high optical transparency in the visible range. Such selective infrared absorption combined with high visible transparency is highly desirable for a range of applications, including NIR photodetectors, infrared camouflage, transparent laser welding, thermal-shielding coatings on glass, and transparent electronic devices.[25,49–52]

Cyclic voltammetry (CV) measurements were conducted on thin films of PDPPC$_{20}$OT-C$_8$ and PDPPC$_{12}$OT-C$_{12}$ deposited on platinum electrodes (Fig. 1b). The HOMO energy levels of PDPPC$_{20}$OT-C$_8$ and PDPPC$_{12}$OT-C$_{12}$ were calculated to be −5.06 eV and −5.02 eV, respectively, based on their onset oxidation potentials. Despite the different side chain lengths, the two polymers exhibit very similar HOMO energy levels because these are governed mainly by the electronic structure and effective conjugation length of the same conjugated backbone rather than by the alkyl side chains. The slightly deeper HOMO level of PDPPC$_{20}$OT-C$_8$ may arise from side-chain-induced steric effects that increase backbone twisting and less ordered chain packing, consistent with its slightly larger optical bandgap (0.90 eV *vs.* 0.87 eV).

Owing to the absence of discernible reduction peaks, their LUMO energy levels were derived by subtracting the optical band gaps (E_g^{opt}) from the HOMO energy levels, yielding values of −4.03 and −4.05 eV, respectively. It should be noted that the LUMO energy levels estimated in this way may be significantly lower than the actual values because organic semiconductors typically exhibit large exciton binding energies, often around 0.3 eV or higher.[53,54]

3.3 Density functional theory (DFT) simulations

To gain insight into the molecular geometries and frontier molecular orbitals of PDPPC$_{20}$OT-C$_8$ and PDPPC$_{12}$OT-C$_{12}$, DFT calculations were performed using the Gaussian 09 package at the B3LYP/6-31+G(d,p) level. Monomer and dimer model compounds, DPPC$_1$OT and [DPPC$_1$OT]$_2$, were employed, in which the long alkyl side chains on the alkoxythiophene units and on the nitrogen atoms of the DPP core were replaced with methyl groups to accelerate computation (Fig. 2). For comparison, analogous monomer and dimer models of PDPPT-C$_{20}$, denoted as DPPT and [DPPT]$_2$, were also calculated, in which the 2-octyldodecyl substituents were similarly replaced by methyl groups.

The dihedral angle between the thiophene and DPP units (C–C–C–S), defined as θ_1, and the dihedral angle between adjacent thiophene units in the bithiophene, defined as θ_2, were used to evaluate the backbone conformation. The monomer models, DPPT and DPPC$_1$OT, exhibit θ_1 values of 0.14° and 0.88°, respectively, indicating that both structures are highly coplanar, with DPPT being slightly more planar. Compared with DPPT, DPPC$_1$OT shows elevated frontier energy levels due to the strong electron-donating effect of the methoxy substituent. In particular, the HOMO level increases by 0.14 eV, which facilitates the significantly enhanced oxidative polymerization of M2–M4 relative to M1. In addition, the HOMO–LUMO gap of DPPC$_1$OT decreases by 0.10 eV compared to DPPT primarily due to the significantly elevated HOMO energy level.

The dimer [DPPT]$_2$ exhibits θ_1 and θ_2 values of 7.2° and 6.5°, respectively, which are substantially larger than those of [DPPC$_1$OT]$_2$ ($\theta_1 = 1.3°$ and $\theta_2 = 0.17°$). The markedly reduced θ_2 in [DPPC$_1$OT]$_2$ is attributed to conformational locking of the bithiophene segment induced by intramolecular S···O interactions[55] at a distance of 2.81 Å. In contrast, such interactions are absent in [DPPT]$_2$, resulting in a more twisted backbone. Notably, θ_1 in [DPPC$_1$OT]$_2$ increases only slightly relative to the monomer, whereas [DPPT]$_2$ shows a pronounced increase in θ_1 relative to monomer, indicating a strong disruption of backbone coplanarity upon chain extension. The enhanced coplanarity of [DPPC$_1$OT]$_2$ promotes more effective π-conjugation and contributes to band-gap narrowing in the alkoxy-substituted polymers.

The calculated HOMO and LUMO energy levels are −4.83 and −2.87 eV for [DPPT]$_2$ and −4.49 and −2.73 eV for [DPPC$_1$OT]$_2$, respectively, corresponding to band gaps of 1.96 and 1.76 eV. These results indicate that the incorporation of alkoxy substituents significantly raises the HOMO energy level and narrows the band gap. The computational trends are consistent with the experimentally observed electrochemical and optical properties of PDPPC$_{20}$OT-C$_8$, PDPPC$_{12}$OT-C$_{12}$, and PDPPT-C$_{20}$, as well as related analogues bearing different alkyl side chains on the DPP units.[34,35,56]

3.4 Film microstructure analyses

To investigate the thin-film microstructure of PDPPC$_{20}$OT-C$_8$ and PDPPC$_{12}$OT-C$_{12}$, X-ray diffraction (XRD) and atomic force microscopy (AFM) measurements were carried out on thin films deposited on Si/SiO$_2$ substrates. Two-dimensional X-ray diffraction (2D-XRD) was employed to evaluate the crystallinity and molecular packing of thin films annealed at different temperatures (Fig. 3, Fig. S2, and S3).

For PDPPC$_{20}$OT-C$_8$, both the out-of-plane and in-plane patterns show no discernible diffraction peaks in the as-cast state or after annealing up to 200 °C, indicating a predominantly amorphous microstructure. Upon annealing at 250 °C, a weak lamellar (100) reflection appears in the out-of-plane direction at $2\theta = 6.73°$, corresponding to a d-spacing of 13.1 Å, along with a broad π–π stacking (010) peak at $2\theta = 23.8°$ ($d = 3.7$ Å). These features suggest the onset of limited molecular ordering only at elevated temperatures.

In contrast, PDPPC$_{12}$OT-C$_{12}$ exhibits a distinct lamellar (100) peak at $2\theta = 8.0°$, corresponding to a d-spacing of 11.1 Å, together with a broad (010) peak at $2\theta = 23.8°$ ($d = 3.7$ Å) in the out-of-plane pattern of the as-cast film. After annealing at 100 °C, the lamellar peak shifts slightly to $2\theta = 7.6°$ ($d = 11.6$ Å) and increases in intensity, indicating enhanced crystallinity. Further annealing at 150, 200, and 250 °C induces no significant additional changes in the diffraction patterns, suggesting that the film microstructure is largely stabilized after mild thermal treatment.

Compared with DPPT-based homopolymers bearing unsubstituted thiophene units, which typically exhibit high crystallinity,[56]

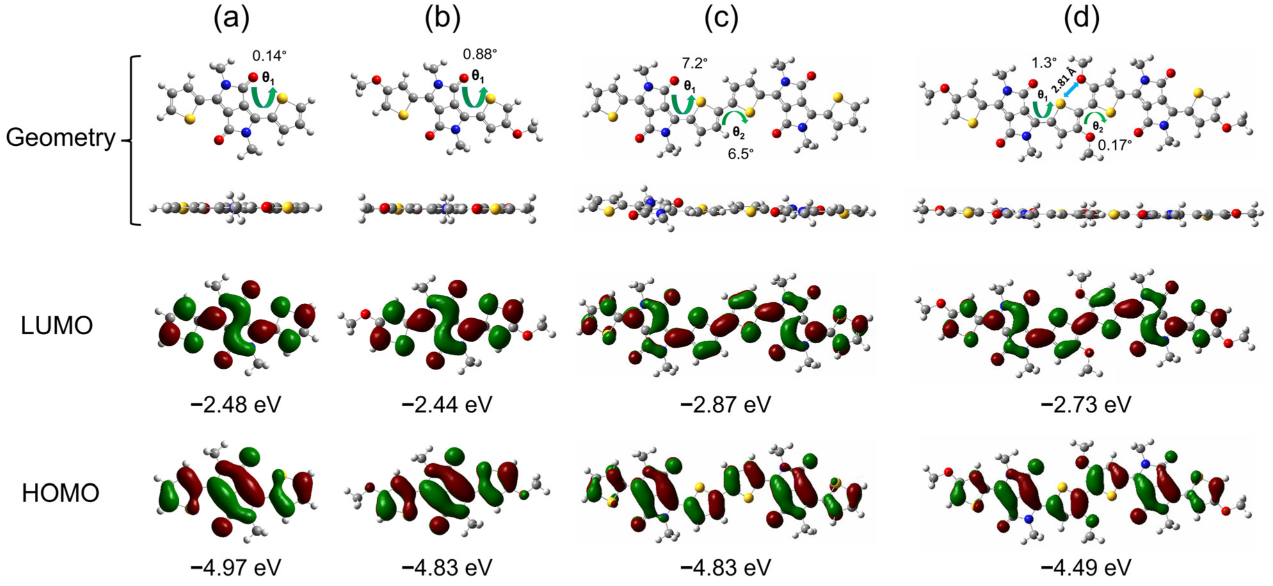

Fig. 2 DFT-optimized geometries and frontier molecular orbitals of model compounds: (a) monomer of PDPPT-C$_{20}$ (DPPT); (b) monomer of PDPPC$_{20}$OT-C$_8$/PDPPC$_{12}$OT-C$_{12}$ (DPPC$_1$OT); (c) dimer of PDPPT-C$_{20}$ ([DPPT]$_2$); and (d) dimer of PDPPC$_{20}$OT-C$_8$/PDPPC$_{12}$OT-C$_{12}$ ([DPPC$_1$OT]$_2$). Long alkyl side chains were replaced with methyl groups in the model structures to reduce computation time.

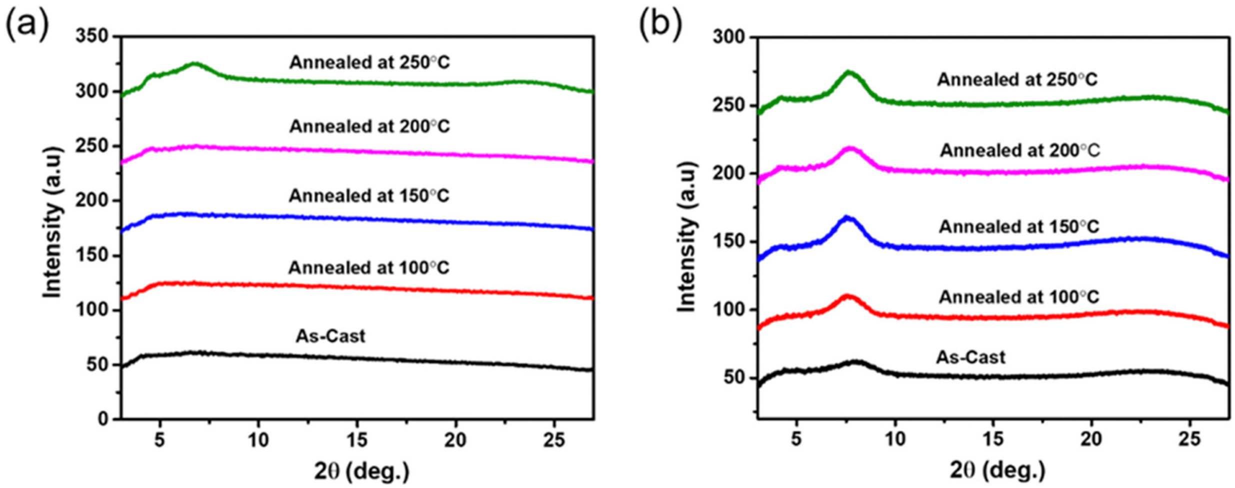

Fig. 3 Out-of-plane XRD patterns of (a) PDPPC$_{20}$OT-C$_8$ (b) PDPPC$_{12}$OT-C$_{12}$.

the present results indicate that alkoxy substitution on the thiophene units hinders efficient chain packing. In particular, the long branched 2-octyldodecyloxy side chains in PDPPC$_{20}$OT-C$_8$ substantially suppress long-range order, whereas the linear octyloxy side chains in PDPPC$_{12}$OT-C$_{12}$ partially preserve lamellar ordering.

To evaluate the surface morphology of the polymer thin films, tapping-mode atomic force microscopy (AFM) measurements were performed, and height images were collected for both polymers in the as-cast state and after thermal annealing (Fig. 4). PDPPC$_{20}$OT-C$_8$ exhibits root mean-square (RMS)

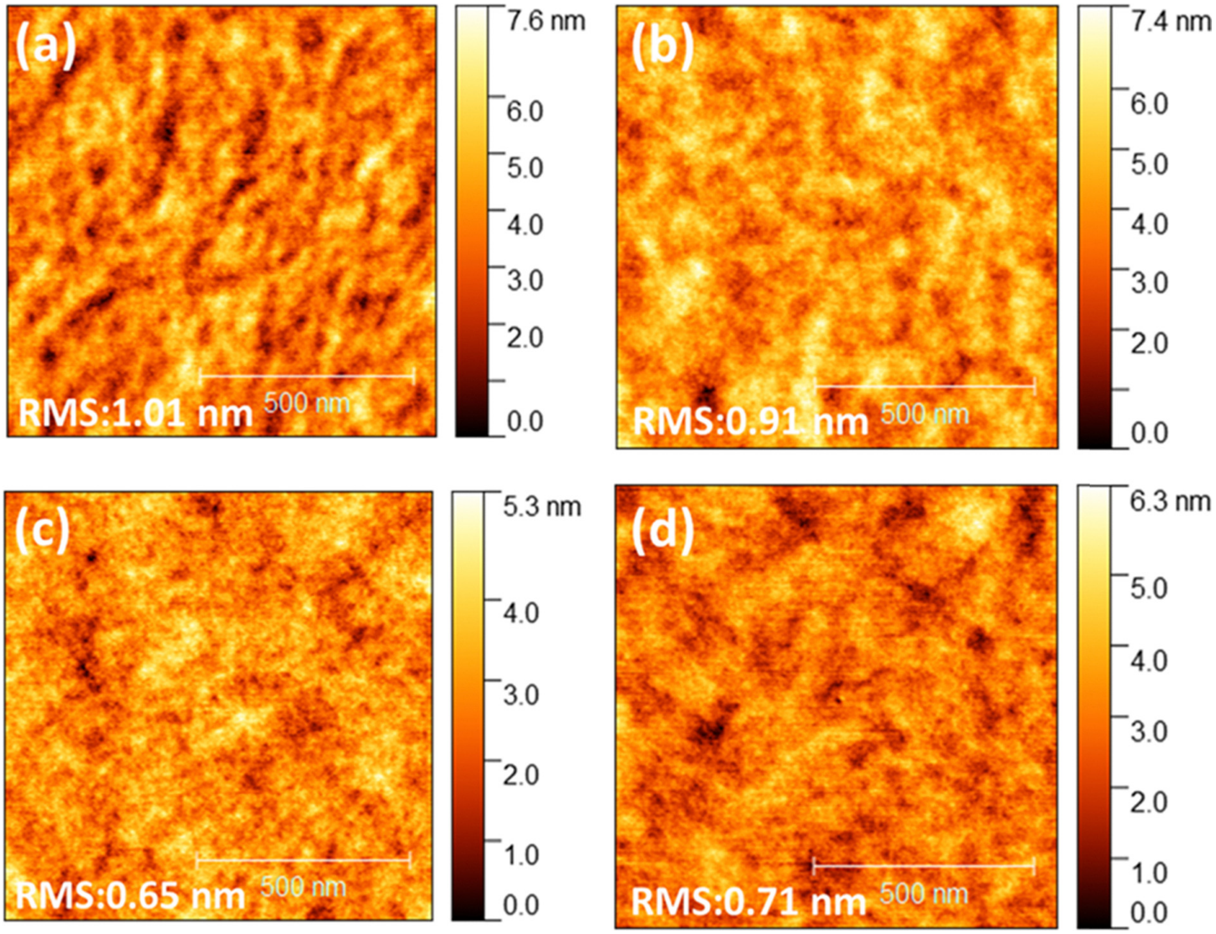

Fig. 4 AFM height images (1 μm × 1 μm) of (a) PDPPC$_{20}$OT-C$_8$ (as-cast) (b) PDPPC$_{20}$OT-C$_8$ (annealed at 200 °C) (c) PDPPC$_{12}$OT-C$_{12}$ (as-cast) (d) PDPPC$_{12}$OT-C$_{12}$ (annealed at 250 °C).

roughness values of 1.01 nm for the as-cast film and 0.91 nm for the film after annealing at 200 °C. In comparison, PDPPC$_{12}$OT-C$_{12}$ shows RMS roughness values of 0.65 nm in the as-cast state and 0.71 nm after annealing at 250 °C. The lower RMS roughness of PDPPC$_{12}$OT-C$_{12}$ indicates that it forms a smoother film surface than PDPPC$_{20}$OT-C$_8$. Nonetheless, both homopolymers exhibit RMS roughness values of 1 nm or less, indicating the formation of uniform and smooth films, which is favorable for improving interfacial contact between the dielectric and semiconducting layers in organic thin-film transistor devices.

3.5 OTFT performance

To evaluate the charge transport properties of the newly synthesized PDPPC$_{20}$OT-C$_8$ and PDPPC$_{12}$OT-C$_{12}$, bottom-gate/bottom-contact (BG/BC) OTFT devices were fabricated on heavily doped silicon substrates with a 300 nm thermally grown SiO$_2$ dielectric layer. The Si/SiO$_2$ substrates were first cleaned using deionized water, acetone, and isopropanol, and then modified with a self-assembled monolayer of dodecyltrichlorosilane. This treatment helps reduce interfacial trap density and adjusts the surface energy, which in turn supports a favorable edge-on molecular orientation and improved π–π stacking at the dielectric interface.[57] The polymer was dissolved in chloroform (10 mg mL^{-1}) and spin-coated at 2000 rpm for 80 s to obtain smooth and uniform thin films with controlled aggregation, typically around 50–60 nm thick. These films were then thermally annealed at temperatures ranging from 100 to 250 °C to further improve molecular ordering and π–π stacking before electrical measurements.

Representative output and transfer curves are shown in Fig. 5, and the extracted charge carrier mobilities in the saturation regime are summarized in Table 2. Both PDPPC$_{20}$OT-C$_8$ and PDPPC$_{12}$OT-C$_{12}$ exhibit typical p-type and n-type transistor behavior at their respective optimal annealing temperatures, indicating ambipolar charge transport.

For PDPPC$_{20}$OT-C$_8$, the device annealed at 200 °C shows the best overall performance, with a highest hole mobility of 6.83×10^{-4} cm^2 V^{-1} s^{-1} (average: $6.05 \times 10^{-4} \pm 1.1 \times 10^{-4}$) and a highest electron mobility of 5.74×10^{-4} cm^2 V^{-1} s^{-1} (average: $5.11 \times 10^{-4} \pm 9.8 \times 10^{-5}$) (Table 2). In comparison, PDPPC$_{12}$OT-C$_{12}$ achieves highest hole and electron mobilities of 1.74×10^{-3} cm^2 V^{-1} s^{-1} (average: $1.66 \times 10^{-3} \pm 1.3 \times 10^{-4}$) and 2.24×10^{-3} cm^2 V^{-1} s^{-1} (average: $2.14 \times 10^{-3} \pm 1.3 \times 10^{-4}$), respectively, at annealing temperature of 250 °C. No measurable electron transport is observed for PDPPC$_{12}$OT-C$_{12}$ in the as-cast state or after annealing at temperatures up to

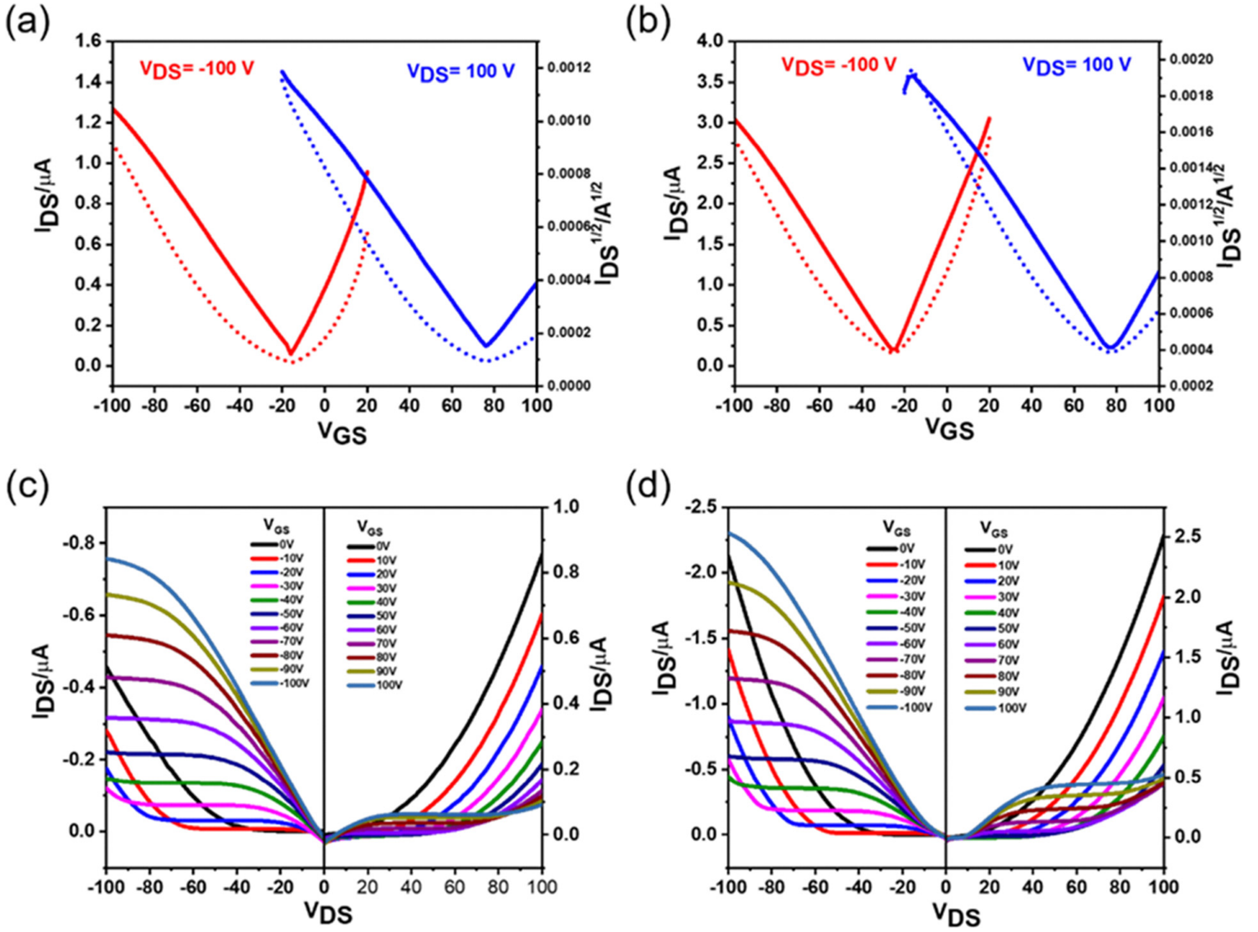

Fig. 5 Representative transfer and output characteristics of OTFT devices fabricated from (a) and (c) PDPPC$_{20}$OT-C$_8$ after annealing at 200 °C and (b) and (d) PDPPC$_{12}$OT-C$_{12}$ after annealing at 250 °C.

Table 2 OTFT device data of homo polymers PDPPC$_{20}$OT-C$_8$ and PDPPC$_{12}$OT-C$_{12}$ thin films, before and after annealing at different temperatures

Homo polymer	Annealing temperature [°C]	Max. μ_h[a] [$cm^2\ V^{-1}\ s^{-1}$]	Avg. μ_h[b] ± Std [$cm^2\ V^{-1}\ s^{-1}$]	Max. μ_e[a] [$cm^2\ V^{-1}\ s^{-1}$]	Avg. μ_e[b] ± Std [$cm^2\ V^{-1}\ s^{-1}$]	I_{on}/I_{off}[c] hole/electron	V_{th}[d] [V] hole/electron
PDPPC$_{20}$OT-C$_8$	As-cast	1.93×10^{-4}	$1.69 \times 10^{-4} \pm 2.4 \times 10^{-5}$	3.32×10^{-4}	$2.63 \times 10^{-4} \pm 7.9 \times 10^{-5}$	$10^2/10^1$	24.0/72.1
	100	1.82×10^{-4}	$1.71 \times 10^{-4} \pm 9.3 \times 10^{-6}$	3.56×10^{-4}	$3.19 \times 10^{-4} \pm 3.2 \times 10^{-5}$	$10^2/10^1$	9.7/69.7
	150	2.95×10^{-4}	$2.61 \times 10^{-4} \pm 3.0 \times 10^{-5}$	3.82×10^{-4}	$3.35 \times 10^{-4} \pm 4.1 \times 10^{-5}$	$10^2/10^1$	−1.8/64.9
	200	6.83×10^{-4}	$6.05 \times 10^{-4} \pm 1.1 \times 10^{-4}$	5.74×10^{-4}	$5.11 \times 10^{-4} \pm 9.8 \times 10^{-5}$	$10^2/10^1$	−5.2/62.8
	250	5.86×10^{-4}	$5.74 \times 10^{-4} \pm 1.7 \times 10^{-5}$	3.44×10^{-4}	$3.39 \times 10^{-4} \pm 5.4 \times 10^{-6}$	$10^2/10^1$	−4.2/61.1
PDPPC$_{12}$OT-C$_{12}$	As-cast	1.27×10^{-3}	$0.85 \times 10^{-3} \pm 3.8 \times 10^{-4}$	—	—	10^2/—	51.4/—
	100	0.86×10^{-3}	$0.82 \times 10^{-3} \pm 4.5 \times 10^{-4}$	—	—	10^2/—	23.7/—
	150	1.23×10^{-3}	$1.17 \times 10^{-3} \pm 7.4 \times 10^{-5}$	—	—	10^2/—	16.9/—
	200	1.57×10^{-3}	$1.43 \times 10^{-3} \pm 1.6 \times 10^{-4}$	1.57×10^{-3}	$1.31 \times 10^{-3} \pm 3.0 \times 10^{-4}$	$10^1/10^0$	3.2/65.6
	250	1.74×10^{-3}	$1.66 \times 10^{-3} \pm 1.3 \times 10^{-4}$	2.24×10^{-3}	$2.14 \times 10^{-3} \pm 1.3 \times 10^{-4}$	$10^1/10^1$	−4.9/59.9

[a] The maximum hole/electron mobility in the saturated region (Max. μ_h/μ_e). [b] The average hole mobility in the saturated region and standard deviation (std) from more than 5 devices. [c] The on-current (I_{on}) to off-current (I_{off}) ratio. [d] The average threshold voltage (V_{th}).

150 °C, which may be attributed to the presence of a high density of electron traps in the thin films (Table 2).

Overall, PDPPC$_{12}$OT-C$_{12}$ exhibits higher charge carrier mobilities compared to PDPPC$_{20}$OT-C$_8$, which is is likely associated with its improved chain packing and smoother film morphology, as evidenced by XRD and AFM analyses (Fig. 3 and 4).

Gold contacts were used in this study. Their work function of approximately −5.0 eV is well aligned with the HOMO energy levels of PDPPC$_{20}$OT-C$_8$ and PDPPC$_{12}$OT-C$_{12}$, but poorly aligned with their LUMO energy levels, resulting in large barriers for electron injection. This may account for the large threshold voltages (V_{th}) observed for n-channel operation (Table 2). Using an electrode material with a higher Fermi energy level or modifying the surface of the Au electrodes[58–61] may facilitate electron injection and thereby reduce the threshold voltage.

To assess device operational stability in ambient air, OTFTs based on PDPPC$_{20}$OT-C$_8$ and PDPPC$_{12}$OT-C$_{12}$ annealed at their optimal temperatures 200 °C and 250 °C, respectively, in the glove box were characterized under ambient conditions (22 °C, 50% relative humidity) (Fig. S7 and Table S1). While their hole-transport performance remained largely stable ($\mu = 1.27 \times 10^{-3}$ $cm^2\ V^{-1}\ s^{-1}$ for PDPPC$_{20}$OT-C$_8$ and 1.58×10^{-3} $cm^2\ V^{-1}\ s^{-1}$ for PDPPC$_{12}$OT-C$_{12}$), their electron transport performance vanished when characterized in ambient air. As noted earlier, the actual LUMO energy levels of these polymers may be significantly higher than the values estimated by combining the HOMO energy level measured by CV with the optical bandgap, owing to their large exciton binding energies. Consequently, their actual LUMO energy levels may exceed the threshold required for air-stable electron transport, which is typically around −4.0 eV.[62,63]

4. Conclusions

In summary, we have demonstrated a cost-effective and scalable approach to ultralow-band-gap DPP homopolymers using FeCl$_3$-mediated oxidative polymerization. Through rational side-chain engineering of alkoxythiophene-flanked DPP monomers, two soluble homopolymers, PDPPC$_{20}$OT-C$_8$ and PDPPC$_{12}$OT-C$_{12}$, were successfully synthesized without the need for expensive transition-metal catalysts. Both polymers exhibit strong NIR-II absorption beyond 1000 nm with optical band gaps as low as 0.87 eV and HOMO energy levels below −5.0 eV, indicating favorable ambient stability. Structural, spectroscopic, and computational analyses reveal that intramolecular S···O interactions enhance backbone planarity and effective π-conjugation, while side-chain architecture governs solid-state packing. As a result, both polymers display ambipolar charge transport in organic thin-film transistors, with PDPPC$_{12}$OT-C$_{12}$ achieving balanced hole and electron mobilities on the order of 10^{-3} $cm^2\ V^{-1}\ s^{-1}$. These results validate oxidative polymerization as a powerful method for accessing NIR-II-active conjugated polymers and provide design guidelines for future low-band-gap materials targeting ambipolar electronics, NIR-II bioimaging, and photothermal conversion.

Author contributions

S. V.: conceptualization, methodology, investigation, validation, formal analysis, visualization, software, writing – original draft. R. S.: methodology, investigation, formal analysis. S. C.: methodology, investigation, formal analysis. A. S.: methodology, investigation, formal analysis. J. P.: methodology, investigation, formal analysis. N. Z.: methodology, investigation, formal analysis. Y. Y.: methodology, investigation, formal analysis. H. L.: methodology, formal analysis. X. L.: methodology, formal analysis. J. W.: methodology, formal analysis. Y. L.: conceptualization, supervision, investigation, visualization, validation, funding acquisition, investigation, writing – review & editing.

Conflicts of interest

There are no conflicts to declare.

Data availability

All data supporting the findings of this study are available within the article and its supplementary information (SI). Supplementary information: detailed monomer synthesis procedures, OTFT device fabrication and characterization, general experimental methods, thermogravimetric analysis (TGA) curves, GIXRD patterns, GPC traces, ^{1}H and ^{13}C NMR spectra, and mass spectrometry data. See DOI: https://doi.org/10.1039/d6ma00031b.

Acknowledgements

We acknowledge support from Defence Research and Development Canada's Centre for Security Science and Public Safety Canada through The Canadian Safety and Security Program CSSP-2022-CP-2544.

Notes and references

1 G. Kim, S.-J. Kang, G. K. Dutta, Y.-K. Han, T. J. Shin, Y.-Y. Noh and C. Yang, *J. Am. Chem. Soc.*, 2014, **136**, 9477–9483.

2 N. A. Kukhta and C. K. Luscombe, *Chem. Commun.*, 2022, **58**, 6982–6997.

3 L. Lu, T. Zheng, Q. Wu, A. M. Schneider, D. Zhao and L. Yu, *Chem. Rev.*, 2015, **115**, 12666–12731.

4 S. B. Mdluli, M. E. Ramoroka, S. T. Yussuf, K. D. Modibane, V. S. John-Denk and E. I. Iwuoha, *Polymers*, 2022, **14**, 716.

5 M. Ni, Z. Zhuo, B. Liu, X. Han, J. Yang, L. Sun, Y. Yang, J. Cai, X. An, L. Bai, M. Xu, J. Lin, Q. Feng, G. Xie, Y. Wu and W. Huang, *Nat. Commun.*, 2025, **16**, 330.

6 M. Pandey, N. Kumari, S. Nagamatsu and S. S. Pandey, *J. Mater. Chem. C*, 2019, **7**, 13323–13351.

7 X. Tu, X. Yao, Y. Li, S. Zhang, Z. He, C. Zhang, Z. Liu, H. Zhong and Z. Fei, *ACS Appl. Polym. Mater.*, 2024, **6**, 5970–5979.

8 L. Yu, X. Xing, D. Fang and H. Meng, *Adv. Opt. Mater.*, 2022, **10**, 2201423.

9 A. Facchetti, *Chem. Mater.*, 2011, **23**, 733–758.

10 K. Müllen and U. Scherf, *Macromol. Chem. Phys.*, 2023, **224**, 2200337.

11 J. Wu, L. You, L. Lan, H. J. Lee, S. T. Chaudhry, R. Li, J. Cheng and J. Mei, *Adv. Mater.*, 2017, **29**, 1703403.

12 J. Vanderspikken, Q. Liu, Z. Liu, T. Vandermeeren, T. Cardeynaels, S. Gielen, B. Van Mele, N. Van Den Brande, B. Champagne, K. Vandewal and W. Maes, *Adv. Funct. Mater.*, 2022, **32**, 2108146.

13 J. Li, L. Xie, W. Sang, W. Li, G. Wang, H. Tian, Z. Zhang, J. Liu, Q. Fan and Y. Dai, *ChemPhysMater*, 2022, **1**, 51–55.

14 M. C. Scharber and N. S. Sariciftci, *Adv. Mater. Technol.*, 2021, **6**, 2000857.

15 H. Chen, Y. Guo, G. Yu, Y. Zhao, J. Zhang, D. Gao, H. Liu and Y. Liu, *Adv. Mater.*, 2012, **24**, 4618–4622.

16 J.-M. Park, S. K. Park, W. S. Yoon, J. H. Kim, D. W. Kim, T.-L. Choi and S. Y. Park, *Macromolecules*, 2016, **49**, 2985–2992.

17 Z. Zhao, Z. Yin, H. Chen, L. Zheng, C. Zhu, L. Zhang, S. Tan, H. Wang, Y. Guo, Q. Tang and Y. Liu, *Adv. Mater.*, 2017, **29**, 1602410.

18 J. Yuan, C. McDowell, C.-K. Mai, G. C. Bazan and W. Ma, *Chem. Mater.*, 2016, **28**, 7479–7486.

19 J. D. Yuen and F. Wudl, *Energy Environ. Sci.*, 2013, **6**, 392.

20 G. Zhang, J. Chen, Y. Dai, S. Song, Z. Ye, H. Lu, L. Qiu and K. Cho, *Dyes Pigm.*, 2017, **137**, 221–228.

21 L. Dou, Y. Liu, Z. Hong, G. Li and Y. Yang, *Chem. Rev.*, 2015, **115**, 12633–12665.

22 K. Welsher, Z. Liu, S. P. Sherlock, J. T. Robinson, Z. Chen, D. Daranciang and H. Dai, *Nat. Nanotechnol.*, 2009, **4**, 773–780.

23 F. Ding, Y. Zhan, X. Lu and Y. Sun, *Chem. Sci.*, 2018, **9**, 4370–4380.

24 G. Hong, A. L. Antaris and H. Dai, *Nat. Biomed. Eng.*, 2017, **1**, 0010.

25 T. Zubair, M. M. Hasan, R. S. Ramos and R. M. Pankow, *J. Mater. Chem. C*, 2024, **12**, 8188–8216.

26 J. C. Bijleveld, A. P. Zoombelt, S. G. J. Mathijssen, M. M. Wienk, M. Turbiez, D. M. De Leeuw and R. A. J. Janssen, *J. Am. Chem. Soc.*, 2009, **131**, 16616–16617.

27 Y. Li, P. Sonar, L. Murphy and W. Hong, *Energy Environ. Sci.*, 2013, **6**, 1684.

28 J. D. Girase, I.-C. Kim and Y.-H. Kim, *Energy Mater.*, 2025, **5**, 500132.

29 I. Kang, H.-J. Yun, D. S. Chung, S.-K. Kwon and Y.-H. Kim, *J. Am. Chem. Soc.*, 2013, **135**, 14896–14899.

30 J. D. Yuen, J. Fan, J. Seifter, B. Lim, R. Hufschmid, A. J. Heeger and F. Wudl, *J. Am. Chem. Soc.*, 2011, **133**, 20799–20807.

31 C. B. Nielsen, M. Turbiez and I. McCulloch, *Adv. Mater.*, 2013, **25**, 1859–1880.

32 P. K. Upputuri, *J. Biomed. Opt.*, 2018, **24**, 1.

33 W. Khelifi, H. Awada, S. Blanc, G. H. Roche, L. Hirsch, B. Oboho, F. Castet, A. Bousquet and C. Lartigau-Dagron, *Appl. Sci.*, 2022, **12**, 4494.

34 A. Domokos, S. D. Aronow, T. Tang, N. E. Shevchenko, D. J. Tantillo and A. S. Dudnik, *ACS Omega*, 2019, **4**, 9427–9433.

35 D. Giri, S. K. Saha, I. Anderson, A. Chakraborty, J. Kala, J. S. Müller, J. Nelson, R. K. Canjeevaram Balasubramanyam and S. Patil, *Adv. Funct. Mater.*, 2025, **35**, 2410815.

36 D. D. Hebert, M. A. Naley, C. C. Cunningham, D. J. Sharp, E. E. Murphy, V. Stanton and J. A. Irvin, *Materials*, 2021, **14**, 6146.

37 T. Cai, Y. Zhou, E. Wang, S. Hellström, F. Zhang, S. Xu, O. Inganäs and M. R. Andersson, *Sol. Energy Mater. Sol. Cells*, 2010, **94**, 1275–1281.

38 R. D. McCullough, *Adv. Mater.*, 1998, **10**, 93–116.

39 M. K. Charyton, T. Reiker, K. Kotwica, M. Góra, H. Zacharias and N. D. Boscher, *Mater. Adv.*, 2023, **4**, 2625–2635.

40 A. Szkurlat, *Electrochim. Acta*, 2003, **48**, 3665–3676.

41 B. Sankaran and J. R. Reynolds, *Macromolecules*, 1997, **30**, 2582–2588.

42 M. Fall, L. Assogba, J.-J. Aaron and M. M. Dieng, *Synth. Met.*, 2001, **123**, 365–372.

43 T. Yamamoto, M. Omote, Y. Miyazaki, A. Kashiwazaki, B.-L. Lee, T. Kanbara, K. Osakada, T. Inoue and K. Kubota, *Macromolecules*, 1997, **30**, 7158–7165.

44 D. Thanasamy, D. Jesuraj, S. K. Konda Kannan and V. Avadhanam, *Polymer*, 2019, **175**, 32–40.

45 M. Más-Montoya and R. A. J. Janssen, *Adv. Funct. Mater.*, 2017, **27**, 1605779.

46 Y.-H. Shih, G.-L. Chen, P.-H. Liu, K.-W. Tseng, W.-Y. Lee, W.-C. Chen, L. Wang and C.-C. Chueh, *ACS Appl. Electron. Mater.*, 2024, **6**, 1797–1808.

47 Y. Li, P. Sonar, S. P. Singh, M. S. Soh, M. Van Meurs and J. Tan, *J. Am. Chem. Soc.*, 2011, **133**, 2198–2204.

48 B. S. Ong, Y. Wu, P. Liu and S. Gardner, *J. Am. Chem. Soc.*, 2004, **126**, 3378–3379.

49 J. Xu, J. Liu and L. Wang, *Angew. Chem., Int. Ed.*, 2023, **62**, e202303870.

50 Y. Huang, Y. Xu, K. Liu, Y. Fu, A. G. Ricciardulli, F. Wang, S. Yang, J. Ma, M. Li, Z. Qian, R. Wang and P. Zhang, *ACS Mater. Lett.*, 2024, **6**, 1069–1076.

51 H. Fu, L. Zhang, Y. Dong, C. Zhang and W. Li, *Mater. Chem. Front.*, 2023, **7**, 2337–2358.

52 Y. Chen, Q. Zhou, X. Liang, B. Hu, S. Zhao, L. Tan and Z. Liu, *ACS Appl. Electron. Mater.*, 2025, **7**, 8583–8591.

53 M. C. Scharber and N. S. Sariciftci, *Adv. Mater. Technol.*, 2021, **6**, 2000857.

54 S. Kashani, J. J. Rech, T. Liu, K. Baustert, A. Ghaffari, I. Angunawela, Y. Xiong, A. Dinku, W. You, K. Graham and H. Ade, *Adv. Energy Mater.*, 2024, **14**, 2302837.

55 G. S. Sinclair, R. C. M. Claridge, A. J. Kukor, W. S. Hopkins and D. J. Schipper, *Chem. Sci.*, 2021, **12**, 2304–2312.

56 Y. Li, B. Sun, P. Sonar and S. P. Singh, *Org. Electron.*, 2012, **13**, 1606–1613.

57 Y. Wu, P. Liu, B. S. Ong, T. Srikumar, N. Zhao, G. Botton and S. Zhu, *Appl. Phys. Lett.*, 2005, **86**, 142102.

58 L.-L. Chua, J. Zaumseil, J.-F. Chang, E. C.-W. Ou, P. K.-H. Ho, H. Sirringhaus and R. H. Friend, *Nature*, 2005, **434**, 194–199.

59 B. Sun, W. Hong, H. Aziz and Y. Li, *Polym. Chem.*, 2015, **6**, 938–945.

60 P. Schulz, T. Schäfer, C. D. Zangmeister, C. Effertz, D. Meyer, D. Mokros, R. D. Van Zee, R. Mazzarello and M. Wuttig, *Adv. Mater. Interfaces*, 2014, **1**, 1300130.

61 X. Peng, L. Hu, F. Qin, Y. Zhou and P. K. Chu, *Adv. Mater. Interfaces*, 2018, **5**, 1701404.

62 H. Yan, Z. Chen, Y. Zheng, C. Newman, J. R. Quinn, F. Dötz, M. Kastler and A. Facchetti, *Nature*, 2009, **457**, 679–686.

63 S. Griggs, A. Marks, H. Bristow and I. McCulloch, *J. Mater. Chem. C*, 2021, **9**, 8099–8128.